Volume 7
Number 4
21 February 2025
Pages 925–1216

Nanoscale Advances

rsc.li/nanoscale-advances

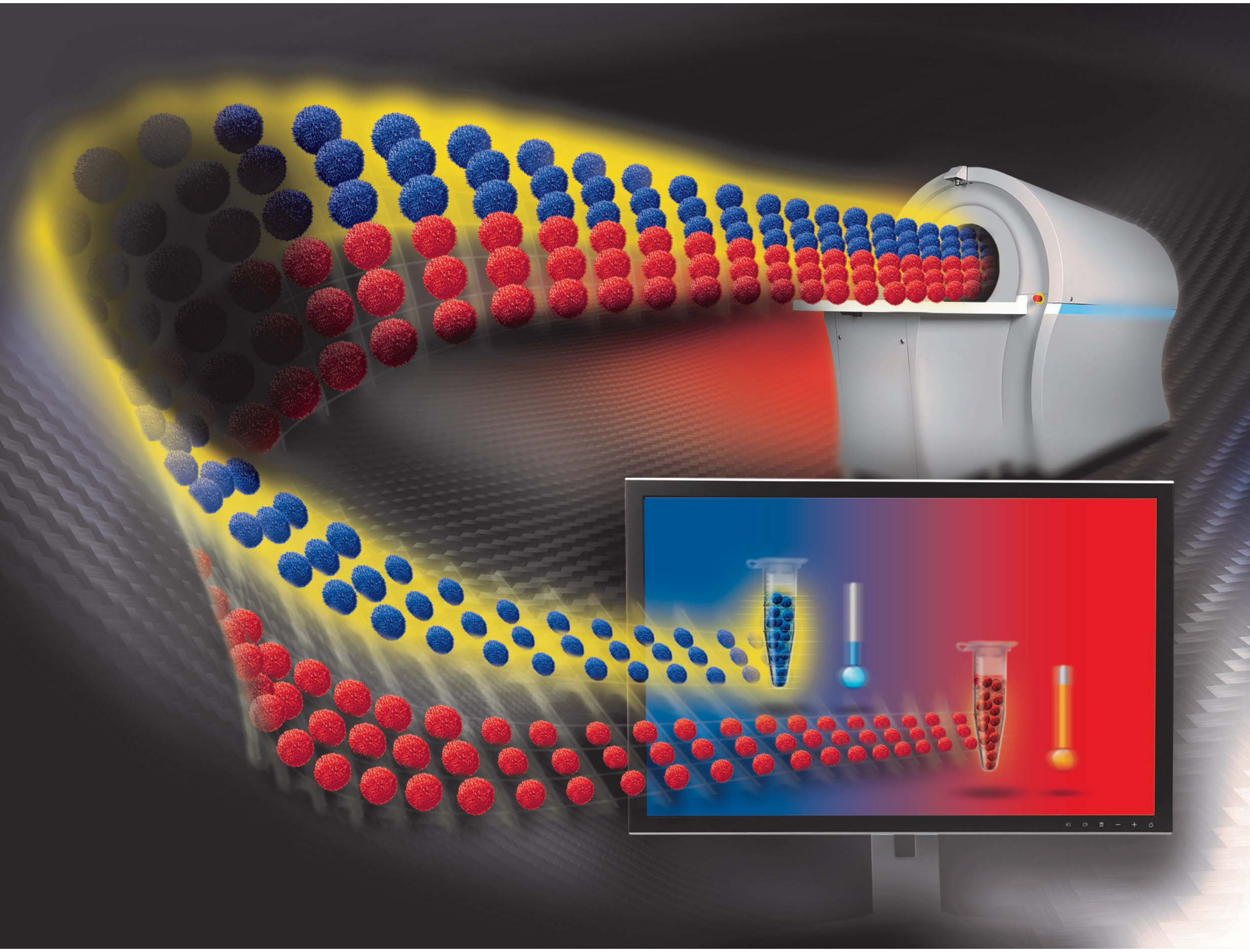

ISSN 2516-0230

PAPER

Jeff W. M. Bulte *et al.*

MPI performance of magnetic nanoparticles depends on matrix composition and temperature: implications for *in vivo* MPI signal amplitude, spatial resolution, and tracer quantification

ROYAL SOCIETY
OF **CHEMISTRY**

NCNST

Nanoscale Advances

ROYAL SOCIETY OF CHEMISTRY

PAPER

View Article Online
View Journal | View Issue

Check for updates

Cite this: *Nanoscale Adv.*, 2025, 7, 1018

MPI performance of magnetic nanoparticles depends on matrix composition and temperature: implications for *in vivo* MPI signal amplitude, spatial resolution, and tracer quantification†

Marzieh Salimi, [ab] Wenshen Wang, [ac] Stéphane Roux, [d] Gautier Laurent, [d] Rana Bazzi, [d] Patrick Goodwill, [e] Guanshu Liu [ac] and Jeff W. M. Bulte *[abcfgh]

One of the hallmark advantages of magnetic particle imaging (MPI) is the linear relationship between MPI signal and the concentration of magnetic nanoparticles (MNPs), allowing absolute tracer quantification. However, intrinsic tissue matrix parameters may affect the MPI signal, often unknown *a priori*, presenting a challenge for accurate *in vivo* MNP quantification in living subjects when using standard calibration curves obtained from simple aqueous MNP suspensions. We investigated the effects of matrix composition and temperature on the MPI signal amplitude and full width at half maximum (FWHM, metric for spatial resolution) for three different MNPs in gelatin and bovine serum albumin (BSA) phantoms and five different *ex vivo* tissues. Decreasing matrix compressibility (increasing viscosity) led to decreased MPI signal amplitude and increased FWHM. For 8% w/v gelatin (compressibility = 3.5×10^{-10} m^2 N^{-1}, viscosity = 363.4×10^3 mPa s), the MPI signal amplitude of MNPs was ∼50% of that in aqueous solutions (compressibility = 8.4×10^{-10} m^2 N^{-1}, viscosity = 1 mPa s), while the FWHM increased by an average of 115%. For 5% w/v BSA samples (compressibility = 1.2×10^{-10} m^2 N^{-1}, viscosity = 198.6×10^3 mPa s), a 44% MPI signal reduction and 98 and 90% increase of FWHM was observed for gold–iron oxide nanoflowers and ferucarbotran, respectively, compared to water (0% w/v). MNPs injected in *ex vivo* tissues also showed lower MPI signal amplitudes compared to aqueous solutions. Temperature also played a small role in MPI quantification, with the MPI signal amplitude of ferucarbotran decreasing by nearly 10% from 55 to 10 °C. The current results suggest that accurate *in vivo* MNP quantification will require reference/calibration samples with matching tissue matrix composition and temperature.

Received 24th June 2024
Accepted 3rd January 2025

DOI: 10.1039/d4na00518j

rsc.li/nanoscale-advances

Introduction

MPI is an emerging imaging modality that detects the magnetic relaxation of magnetic nanoparticles (MNP) to produce high-specificity and high-sensitivity images of MNP-containing tissues.[1] With MNPs acting as imaging tracers instead of contrast agents,[2] MPI enables quantification of the concentration of MNPs for a wide range of biomedical applications, including cell tracking[3,4] and imaging-guided magnetic hyperthermia.[5–8] Some applications, especially cell tracking, rely on the quantitativeness of the technique. However, the MPI signal from iron oxide-labeled cells may differ from the tracer alone, and the peak signal level and image resolution may even change depending on the labeling method. The changing signal complicates quantitation and is hypothesized to be due to changes in particle relaxation.

In MPI, the relaxation time of the magnetization in response to oscillating external magnetic fields is primarily influenced by the rotational speed under torque, due to the presence of a drive field.[9] This torque differs from the Néel relaxation mechanism, which describes the realignment of the magnetic moment inside the magnetic core against an energy barrier without requiring physical rotation, and the Brownian relaxation mechanism, which describes the physical rotation of the particle in the absence of an external field.[10–12] Any parameter

---

[a] Russell H. Morgan Department of Radiology and Radiological Science, Division of MR Research, The Johns Hopkins University, Baltimore, Maryland, USA. E-mail: jwmbulte@mri.jhu.edu

[b] Cellular Imaging Section and Vascular Biology Program, The Johns Hopkins University School of Medicine, Baltimore, Maryland, USA

[c] F. M. Kirby Research Center for Functional Brain Imaging, Kennedy Krieger Inc., Baltimore, MD, USA

[d] Université de Franche-Comté, CNRS, Chrono-Environnement, F-25000, Besançon, France

[e] Magnetic Insight Inc. Alameda, CA, USA

[f] Department of Biomedical Engineering, The Johns Hopkins University School of Medicine, Baltimore, Maryland, USA

[g] Department of Oncology, The Johns Hopkins University School of Medicine, Baltimore, Maryland, USA

[h] Department of Chemical & Biomolecular Engineering, Johns Hopkins University Whiting School of Engineering, USA

† Electronic supplementary information (ESI) available. See DOI: **https://doi.org/10.1039/d4na00518j**

affecting MNP magnetization, and its rotational dynamics under torque can potentially affect their response pattern to the oscillating magnetic field and hence the MPI signal; for example, studies showed that the externally applied magnetic field strength[13] and the size distribution of MNPs[14] can be major determinants of the MPI signal.

For particles that mechanically rotate, the viscosity of the nanoparticle environment can impose rotational drag on magnetic nanoparticles, influencing their relaxation dynamics.[15,16] Previous studies have studied the effects of matrix viscosity on the MPI signal of MNPs and found that increased viscosity can result in extended relaxation times and reduced signal amplitude in MPI. This is due to the restricted rotational mobility of MNPs in higher-viscosity environments.[9,17,18]

We hypothesized that when MNPs are embedded in a less compressible matrix, their response pattern to oscillating magnetic fields is altered compared to aqueous samples, resulting in a different MPI signal, similar to that observed with magnetic fluid hyperthermia (MFH).[19] Matrix compressibility refers here to the ability of MNP-containing materials, such as biological tissue or gel, to undergo volume changes under external pressure. Additionally, temperature changes could also affect the MPI signal by differences in the rotational dynamics of MNPs[6] or by indirectly inducing a change of matrix compressibility itself, which can further exert non-negligible effects on the MPI signal.[20] To the best of our knowledge, no previous study has systematically investigated the effects of matrix compressibility, viscosity and temperature on the MPI signal amplitude and resolution. We performed a comparative study of the MPI signal response of three MNP formulations embedded in gelatin and crosslinked bovine serum albumin (BSA) hydrogels as matrices with different compressibilities and viscosities. The dependence of the MPI signal on temperature study was also studied from 10 °C to 55 °C. It is shown that the results for the hydrogel phantoms corresponded to data obtained for *ex vivo* tissues with different matrix compressibilities.

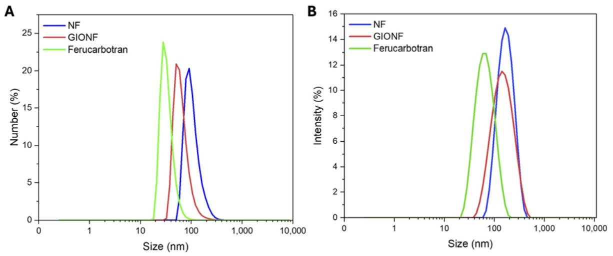

Fig. 1 Hydrodynamic diameter of NF, GIONF, and ferucarbotran as measured by (A) intensity and (B) number-based distribution DLS.

Results

MNP size distribution

Nanoflowers (NF), gold iron oxide NF (GIONF) and ferucarbotran MNPs were used throughout this study. NF are composed of small monocrystalline iron oxide grains assembled in a flower-shaped structure, coated with citrate anions.[21] GIONF is obtained by grafting gold nanoparticles onto NF.[22] Ferucarbotran (the active pharmaceutical ingredient in Resovist®) is a carboxydextran-coated commercial MNP formulation. The hydrodynamic sizes of the three formulations were measured using dynamic light scattering (DLS) and calculated with intensity and number-based distributions (Fig. 1). The mean hydrodynamic size of NF, GIONF, and ferucarbotran was 177 ± 64, 160 ± 76, and 69 ± 29 nm for an intensity-based distribution, and 106 ± 39.4, 65 ± 25, and 33.5 ± 10 nm for a number-based distribution, respectively (ESI Table 1†). Transmission electron microscopy (TEM) (ESI Fig. 1†) confirmed that the particle composition of our specific lots were consistent with those reported in the experimental section based on literature values.

Compressibility of gelatin and BSA hydrogels

To calculate the matrix compressibility of gelatin and BSA, we first measured the ultrasound velocity in these samples. Ultrasound velocity increased with increasing concentration for both gelatin and BSA (Table 1). The highest and lowest ultrasound velocities were measured in 8% w/v gelatin (1646 m s^{-1}) and water (1101 m s^{-1}). Using the measured ultrasound velocity in each phantom, the compressibility was calculated using eqn (4). As expected, the compressibility decreased with increasing gelatin concentration: the compressibility of water (0% w/v gelatin or BSA), was 2.4 and 7 times higher than that for 8% w/v gelatin and 5% w/v BSA hydrogel, respectively.

Table 1 Physical characterization of phantoms containing different gelatin and BSA concentrations. Measurements were performed three times at room temperature

Matrix	Concentration (% w/v)	Ultrasound velocity [m s^{-1}]	Density [kg m^{-3}]	Bulk modulus [GPa]	Compressibility [m^2 N^{-1}]	Viscosity [mPa s]
Gelatin	1	1376 ± 23	994.33	1.88	$5.31 \times 10^{-10} \pm 1.7 \times 10^{-11}$	$0.017 \times 10^3 \pm 0.002 \times 10^3$
	2	1442 ± 13	1012.33	2.10	$4.75 \times 10^{-10} \pm 8.2 \times 10^{-12}$	$12.99 \times 10^3 \pm 8.66 \times 10^3$
	4	1574 ± 33	1023.66	2.53	$3.94 \times 10^{-10} \pm 1.6 \times 10^{-11}$	$96.66 \times 10^3 \pm 10.53 \times 10^3$
	8	1646 ± 32	1056.00	2.86	$3.49 \times 10^{-10} \pm 1.4 \times 10^{-11}$	$363.39 \times 10^3 \pm 95.27 \times 10^3$
BSA	1.5	2019 ± 215	1005.62	4.10	$2.44 \times 10^{-10} \pm 5.2 \times 10^{-11}$	$16.28 \times 10^3 \pm 9.36 \times 10^3$
	2	2144 ± 280	1014.77	4.66	$2.14 \times 10^{-10} \pm 5.6 \times 10^{-11}$	$32.07 \times 10^3 \pm 4.34 \times 10^3$
	3	2703 ± 86	1016.36	7.42	$1.35 \times 10^{-10} \pm 8.6 \times 10^{-12}$	$77.15 \times 10^3 \pm 3.24 \times 10^3$
	4	2825 ± 151	1021.38	8.15	$1.23 \times 10^{-10} \pm 1.3 \times 10^{-11}$	$138.37 \times 10^3 \pm 19.67 \times 10^3$
	5	2877 ± 391	1024.15	8.47	$1.18 \times 10^{-10} \pm 3.2 \times 10^{-11}$	$198.61 \times 10^3 \pm 21.00 \times 10^3$

Viscosity of gelatin and BSA hydrogels

Viscosity measurements of gelatin and BSA hydrogels showed a clear dependence on the respective % w/v values. For gelatin at a shear rate of 4 s^{-1}, the 1% w/v samples had a viscosity of approximately 17 mPa s, whereas the 8% w/v samples measured at 363 × 10^3 mPa s. Similarly, BSA hydrogels exhibited an increase in viscosity with concentration, with 1.5% w/v BSA having a value of 16 × 10^3 mPa s and 5% w/v BSA measuring 199 × 10^3 mPa s (ESI Fig. 2†).

Effect of gelatin compressibility and viscosity on MPI signal amplitude and resolution

The increase in MPI signal was linear with increasing iron concentration and signal intensity decreased with increasing the gelatin concentration for all MNPs tested (Fig. 2A–F). The highest signal intensity was observed in the aqueous solution of MNPs. The highest percentage change in the MPI signal amplitude occurred between 0 to 1% w/v and then 1 to 2% w/v for NF and GIONF (Table 2). Ferucarbotran had a different behavior compared to NF and GIONF showing a small decrease in MPI signal between 0 and 1% w/v gelatin. The ferucarbotran signal continued to decrease for 2, 4, and 8% gelatin, which was not observed at these gelatin concentrations for NF and GIONF (Table 2). The signal FWHM increased with increasing gelatin concentrations for all MNPs tested (Fig. 3A–F). The reference values of signal amplitude and FWHM for the MNPs in water (0% gelatin) are shown in ESI Table 2.†

Table 2 Percentage change of MPI signal amplitude decrease for NF, GIONF, and ferucarbotran for different iron and gelatin concentrations compared to 0% w/v (water) matrix

MNP	Concentration (μg Fe per mL)	1% w/v	2% w/v	4% w/v	8% w/v
NF	25	35.52	55.97	56.43	56.66
	50	42.13	59.88	59.90	60.26
	100	33.38	52.75	49.16	49.99
GIONF	25	41.43	58.24	59.35	61.29
	50	41.36	59.87	57.79	57.24
	100	32.38	45.54	49.14	49.60
Ferucarbotran	25	2.92	19.90	37.03	39.85
	50	−3.60	17.32	30.85	35.95
	100	4.34	26.84	38.01	42.44

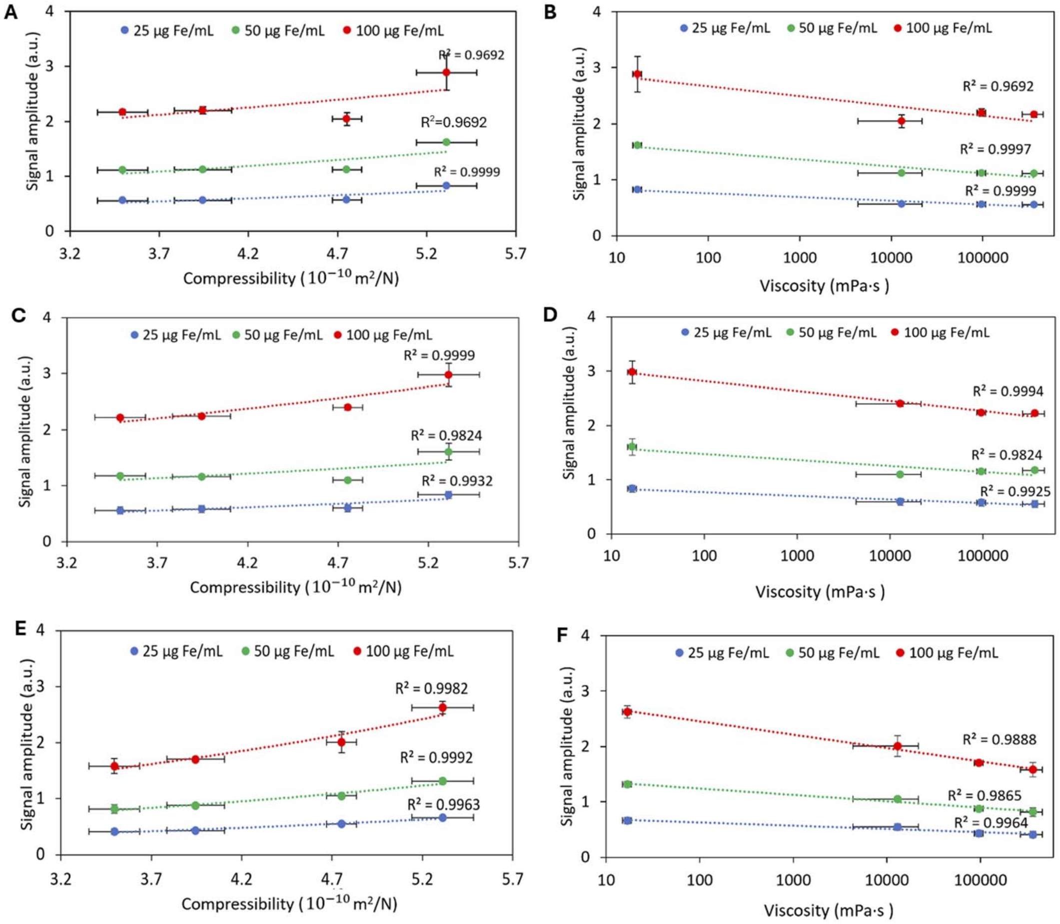

Fig. 2 MPI signal intensity of (A and B) NF, (C and D) GIONF, and (E and F) ferucarbotran in gelatin phantoms with different compressibilities and viscosities. The viscosity values are at shear rate of 4 s^{-1}. Data were obtained at room temperature and are shown as mean ± SD for three independent experiments.

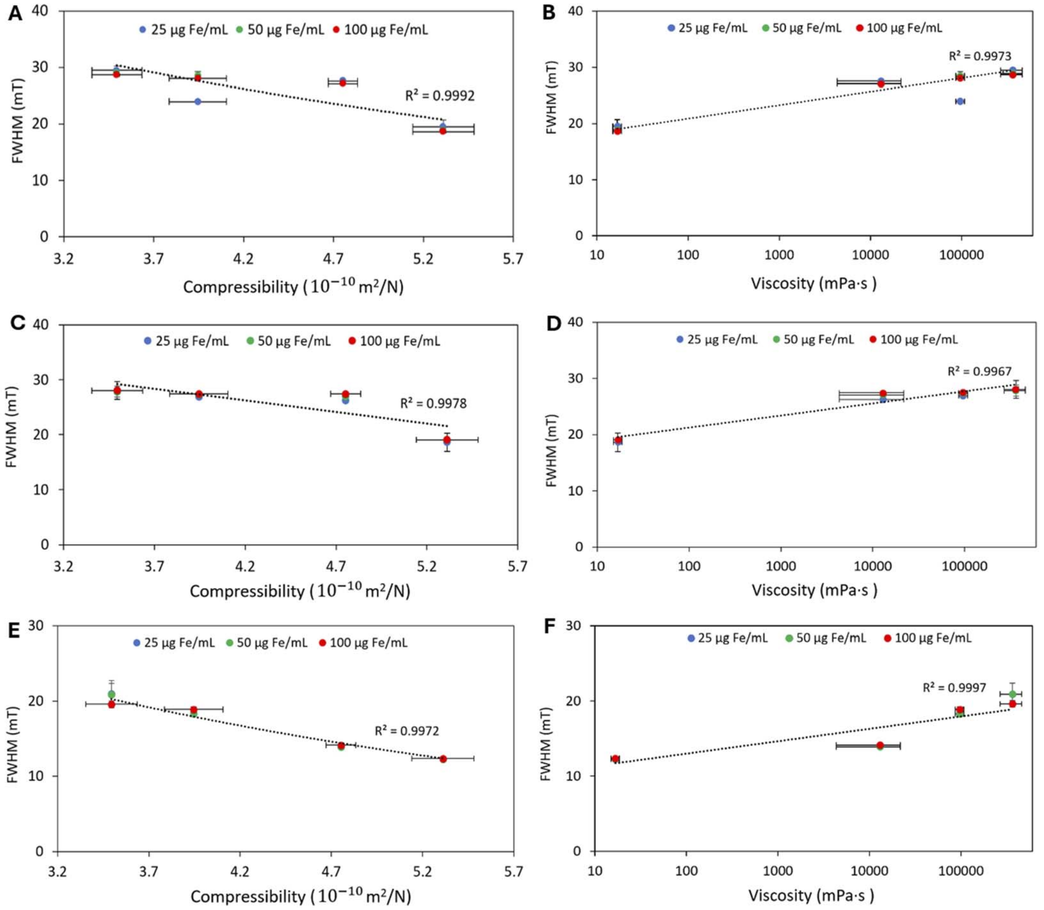

Fig. 3 FWHM values of (A and B) NF, (C and D) GIONF, and (E and F) ferucarbotran in gelatin phantoms with different compressibilities and viscosities. The viscosity values are at a shear rate of 4 s^{-1}. Data were obtained at room temperature and are shown as mean ± SD for three independent experiments.

Effect of BSA compressibility and viscosity on MPI signal amplitude and resolution

The MPI signal amplitude decreased with increasing BSA concentration (decreasing compressibility/increasing viscosity) in phantoms containing GIONF and ferucarbotran (Fig. 4A–D); *e.g.*, the signal amplitude for both GIONF and ferucarbotran decreased by 44% in 5% w/v BSA compared to 1.5% w/v BSA (Table 3). In agreement with the gelatin measurements, increasing the BSA concentration led to an increase in the FWHM values. For GIONF, the FWHM increased 68% in 5% w/v BSA compared to 1.5% w/v. For ferucarbotran, this increase was 48%.

Effect of matrix properties on MPI quantification in *ex vivo* tissues

To validate our *in vitro* findings, we injected the same amounts of GIONF and ferucarbotran into various *ex vivo* tissues with different compressibilities (Fig. 5). The compressibility of PBS, goat brain, lamb kidney, lamb liver, chicken muscle and cow muscle were 8.24, 4.38, 3.90, 3.88, 3.84 and 3.64 × 10^{-10} m^2 N^{-1}, respectively. Fig. 6 shows the MPI signal amplitude and FWHM values for GIONF and ferucarbotran as a function of tissue compressibility. Increasing compressibility led to an increase in MPI signal, consistent with our findings in the gelatin and BSA phantoms. For injection of 100 µg Fe per mL GIONF, the signal amplitude was 0.1 and 0.2 for cow muscle (lowest compressibility) and water (highest compressibility), respectively. For injection of 100 µg Fe per mL ferucarbotran, these values were 0.09 and 0.12, respectively. For GIONF and ferucarbotran injected at 500 µg Fe per mL, the signal amplitude was 0.4 and 0.37 in cow muscle, and 1.3 and 0.6, in water, respectively.

On the other hand, the FWHM increased with decreasing compressibility; the FWHM for cow muscle was 28 mT for GIONF (100 and 500 µg Fe per mL) compared to that in water (13 and 10 mT, respectively). For ferucarbotran (100 and 500 µg Fe per mL), it was 24 and 21 mT for cow muscle and 16 and 13 mT for water, respectively.

Rotational magnetic dynamics of GIONF, ferucarbotran, and fluidMAG-D

The MPI signal amplitude for GIONF and ferucarbotran decreased in dried powder samples compared to aqueous suspensions (Fig. 7) due to losing the external rotational motion component (Brownian relaxation in the presence of a drive field) of the magnetization signal. In contrast, fluidMAG-D nanoparticles did not show a change in signal since these nanoparticles are known to contain only a Néel relaxation

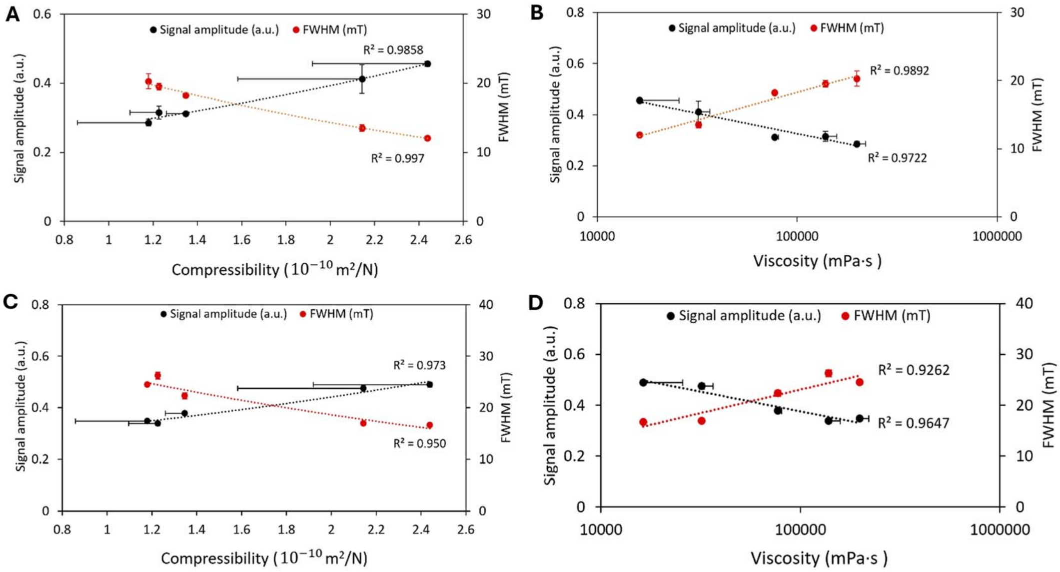

Fig. 4 MPI signal (amplitude and FWHM) for 50 μg Fe per mL GIONF (A and B) and 100 μg Fe per mL ferucarbotran (C and D) in BSA hydrogels with different compressibilities and viscosities. The viscosity values are at a shear rate of 4 s^{-1}. Data were obtained at room temperature and are shown as mean ± SD for three independent experiments.

Table 3 Percentage change of MPI signal amplitude decrease for GIONF and ferucarbotran for different iron and BSA hydrogel concentrations compared to 0% (water) matrix

MNP	Concentration (μg Fe per mL)	1.5% w/v	2% w/v	3% w/v	4% w/v	5% w/v
GIONF	100	9.9	18.63	38.27	37.7	43.46
Ferucarbotran	50	21.2	23.51	39.17	45.5	44.0

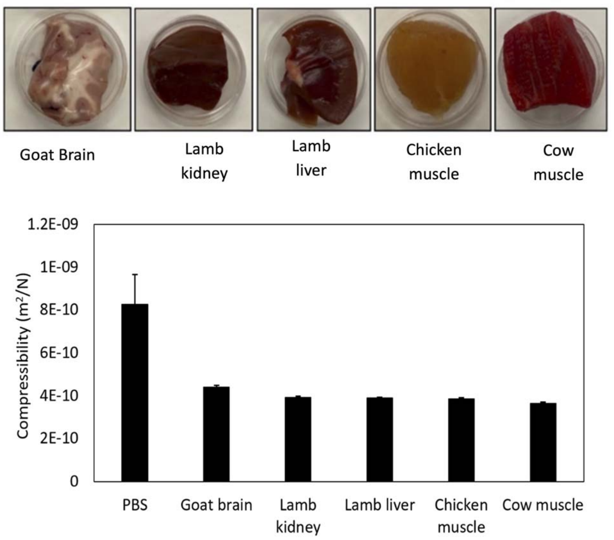

Fig. 5 Measured compressibilities of goat brain, lamb liver, lamb kidney, chicken muscle, and cow muscle. Data were obtained at room temperature and are shown as mean ± SD for three independent experiments.

component.[23] The dried/liquid ratio for GIONF, ferucarbotran, and fluidMAG-D was calculated to be 0.6, 0.5, and 1.0, respectively (Fig. 7).

Effect of temperature on MPI signal amplitude and resolution

The MPI signal intensity of ferucarbotran decreased with increasing water temperature (Fig. 8A). Compared to ambient room temperature (20 °C), the value at 55 °C decreased by 7.6% (Table 4). The increase in FWHM increased with temperature was negligible (15.0 to 15.4 mT, Fig. 8B).

Discussion

Nearly all MPI studies have used MNPs suspended in aqueous solutions as a reference for *in vivo* MPI signal quantification. Similarly, for magnetic resonance imaging (MRI), SPIO proton relaxivities are always reported for non-viscous aqueous solutions but it is known that the T2 relaxivity of SPIOs increases with increasing gelatin concentration/viscosity, corresponding to the measured decrease in the water diffusion coefficient.[24] We therefore undertook a systematic study of the magnetic relaxation properties of MNPs as a function of matrix compressibility and viscosity using two types of gel tissue phantoms as well as different mammalian tissues. Understanding the performance of MNPs in different matrices is crucial for accurate *in vivo* MPI signal quantification. While aqueous solutions have been commonly used as references, they do not fully replicate the conditions of biological tissues. We found that a lower matrix compressibility/higher viscosity

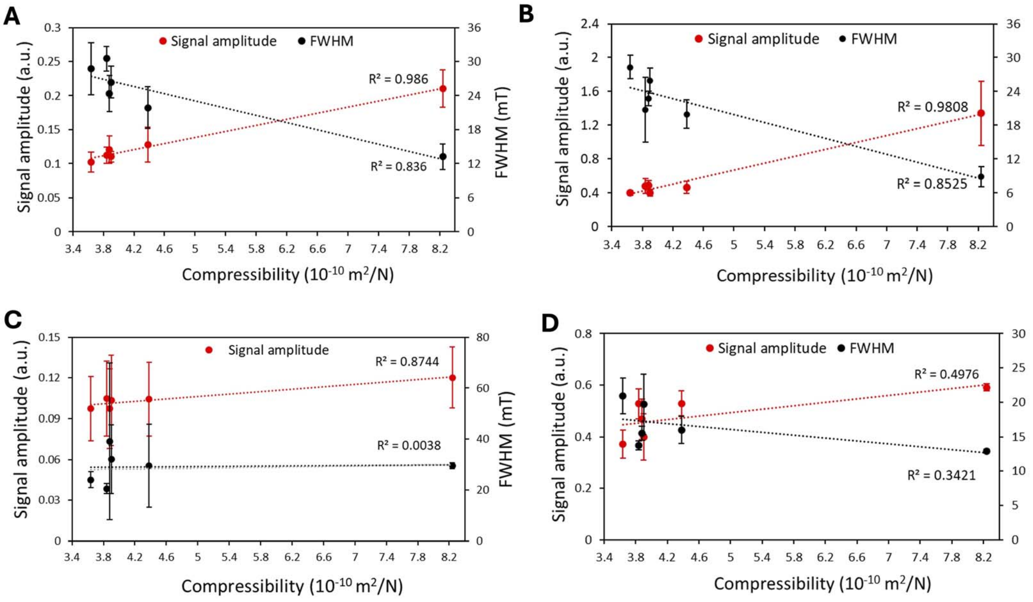

Fig. 6 MPI signal amplitude of tissues with different compressibilities injected with 20 μL of (A) GIONF 100 μg Fe per mL, (B) GIONF 500 μg Fe per mL, (C) ferucarbotran 100 μg Fe per mL and (D) ferucarbotran 500 μg Fe per mL. Data were obtained at room temperature and are shown as mean ± SD for three independent experiments.

was accompanied by a lower MPI signal for both gelatin and BSA phantoms and different tissues. These results are paralleled by previous studies that reported that lower compressibilities of agar phantoms lead to a lower thermal effect in MFH.[19] This is not surprising, as the same magnetic relaxation principles of MNPs apply to MPI and MFH.

By embedding MNPs in phantoms with different gelatin and BSA concentrations, the compressibility/viscosity of the matrix was varied with higher concentrations resulting in a lower compressibility/higher viscosity of the matrix. This is accompanied by an increased reduction of the speed of magnetic relaxation and hence the MPI signal. We showed this to occur for all MNPs at all concentrations. Compressibility, often treated as a macroscopic, phenomenological quantity, describes how a material's volume changes in response to pressure. This is typically measured in terms of isothermal or adiabatic compressibility, using observable variables like volume, pressure, and temperature. However, compressibility also has a solid microscopic foundation. On a microscopic level,

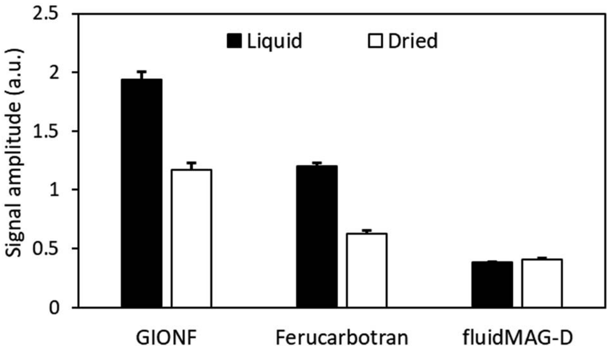

Fig. 7 MPI signal amplitude of liquid and dried (lyophilized powder) GIONF, ferucarbotran, and fluidMAG-D. Data were obtained at room temperature and are shown as mean ± SD for three independent experiments.

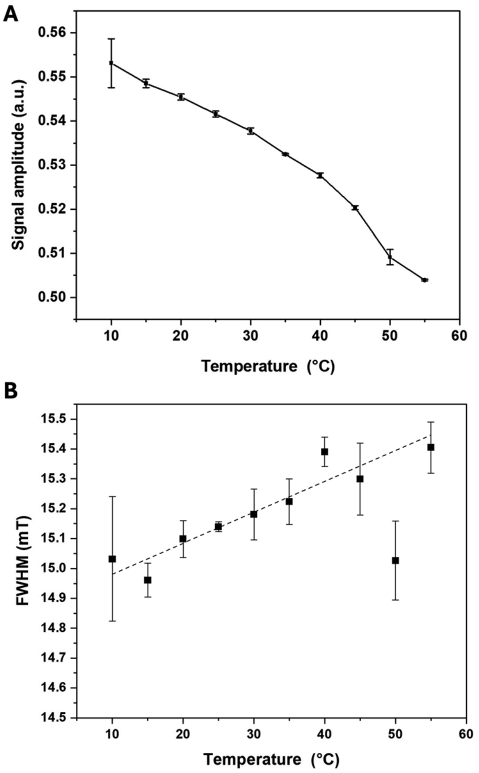

Fig. 8 (A) MPI signal amplitude and (B) FWHM of ferucarbotran (100 μg Fe per mL) at different temperatures (10–55 °C). Data are shown as mean ± SD for three independent experiments.

Table 4 MPI signal amplitude at different temperatures (10–55 °C). The percentage change is given compared to 20 °C

Temperature (°C)	Amplitude (a. u.)	Percentage change	FWHM (mT)
10	0.553	−1.40	15.032
15	0.548	−0.55	14.961
20	0.545	0	15.098
25	0.541	0.70	15.139
30	0.537	1.41	15.180
35	0.532	2.38	15.223
40	0.527	3.27	15.390
45	0.520	4.61	15.229
50	0.509	6.66	15.026
55	0.503	7.62	15.404

it can be understood through the interactions between individual molecules, explained using statistical mechanics and molecular dynamics. While compressibility is usually considered in a bulk, observable sense, it ultimately stems from the collective behavior of countless microscopic particles, showing that it is not purely phenomenological but deeply rooted in fundamental physical principles.[25,26]

Relaxation in MPI is complex and is not captured by the well-known zero-field relaxation times understood as Brownian and Néel relaxation, which can underestimate the actual relaxation times by orders of magnitude.[13] In contrast, MPI focuses on the rotational dynamics of MNPs under torque due to the applied oscillating magnetic field.[9,13,27,28] We found that a larger hydrodynamic diameter results in a slower physical rotation relaxation time. Our DLS results showed that the hydrodynamic size of NF and GIONF was around 170 nm, while it was 69 nm for ferucarbotran. Consequently, the gelatin phantom results showed that by increasing the gelatin content (*i.e.*, decreasing matrix compressibility/increasing viscosity), the decrease of the ferucarbotran magnetic relaxation was 2.9% and 39.8% for 25 μg Fe per mL in 1 and 8% w/v gelatin, respectively, compared to that in water (0% w/v). The percentage change of the MPI signal was 35.5% (1% w/v gelatin) and 56.6% (8% gelatin) for NF, and 41.43 and 61.3% for GIONF compared to the water matrix (Table 2).

In this study, the viscosity of gelatin and BSA hydrogels was measured at different concentrations (ESI Fig. 2†). These samples exhibited shear-thinning behavior (non-Newtonian), where viscosity decreases as the shear rate increases. Higher concentrations of gelatin and BSA lead to greater viscosity (Table 1), thereby imposing more significant rotational drag on the MNPs. As viscosity increases, the rotational motion of MNPs may be restricted, leading to reduced MPI signal intensity and altered spatial resolution (FWHM).[9] Understanding the interplay between viscosity and compressibility provides a comprehensive picture of how different matrix properties affect MPI performance, highlighting the importance of tailored calibration for *in vivo* applications. The viscosity of glycerol (1200–1500 mPa s)[29,30] is higher than that of water (0.89–1 mPa s).[18] However, the MPI signal amplitude and FWHM remained similar for ferucarbotran in both media (ESI Fig. 3†). This can be explained by the interplay between viscosity and hydrodynamic size; while the high viscosity of glycerol could increase rotational drag, we found that the hydrodynamic size of ferucarbotran decreased from 69 nm in water to 32.6 nm in glycerol, based on intensity-based DLS measurements (ESI Fig. 4†). According to the Brownian relaxation time in a non-zero field,[28] the reduction in hydrodynamic volume offsets the effect of increased viscosity, resulting in a relatively stable relaxation time across both media. Additionally, the drive field frequency used in our experiments (45 kHz) might reduce the sensitivity of the MPI signal to viscosity changes, aligning with previous studies showing that higher frequencies diminish viscosity effects on relaxation times.[9,18] Thus, while viscosity can impact MPI signal under certain conditions, compressibility and particle interactions may play a more significant role in our experimental setup.

We used an exponential model to fit our MPI signal amplitude data of gelatin (excluding water phantoms) as function of compressibility because it consistently provided the best fit, indicated by high R^2 values close to 1. Despite the occasional accuracy of a 2nd degree polynomial, the exponential model provided a better fit overall. We chose the percentages of gelatin and BSA based on the levels at which their MPI signals were distinguishable from water. Including lower concentrations of gelatin and BSA in our study was challenging because, at these lower levels, MPI signals become nearly indistinguishable from water, making accurate compressibility measurements more difficult.

The relationship between matrix composition and MPI performance can be further understood by considering the role of mesh size in gelatin and BSA gels. As the concentration of these gels increases, the mesh size decreases, leading to potential hydrodynamic confinement of the MNPs.[31] This confinement can increase the effective rotational drag on the particles, thereby influencing their Brownian relaxation. With higher drag, the rotational freedom of the nanoparticles is reduced, potentially resulting in a slower relaxation process and consequently, a diminished MPI signal. This effect, coupled with the impact of compressibility, can explain some of the variations observed in MPI performance across different compositions. The reduced mesh size and higher drag may be particularly important in higher-concentration gels, where both compressibility and viscosity effects become more pronounced, affecting signal amplitude and spatial resolution.

The percentage change in MPI signal with increasing gelatin compressibility was higher for ferucarbotran compared to NF and GIONF, suggesting a larger external rotational component (Brownian-like motion) responsible for the ferucarbotran MPI signal. To verify this hypothesis, aqueous solutions of ferucarbotran, GIONF, and fluidMAG-D nanoparticles were then dried into powder. FluidMAG-D nanoparticles (50 nm) were included as a reference since their magnetization is solely derived from internal rotational dynamics in both aqueous and dried samples.[15] These particles comprise a single-domain core containing a blend of particles with either a small magnetic moment and short τ_N, or particles with a larger magnetic moment and medium τ_N and τ_B. In general, MNPs cannot respond to an excitation field where the frequency is higher than $1/(2\pi\tau_N)$ or $1/(2\pi\tau_B)$. Consequently, with the excitation frequency set at 20 kHz surpassing $1/(2\pi\tau_B)$, these particles exhibit no Brownian relaxation signal.[23] The results showed that the MPI signal ratio of dried to MNPs suspended in water was 0.6 and 0.52 for GIONF and ferucarbotran, respectively. But, as expected, this ratio remained 1.0 for fluidMAG-D nanoparticles.

The MPI signal intensity also decreased for MNPs injected into tissues with lower compressibilities than PBS. Tissues are expected to have a higher "viscosity", which can however not be measured. Unlike the gel phantoms, the MNP distribution was inhomogeneous, and some particle clustering/agglomeration in tissue may have occurred. Particle aggregation leads to an increase in rotational dynamics of MNPs under torque, resulting in a decrease in the MPI signal.[32–34] On the other hand, aggregation can act as a double-edged sword; studies have shown that aggregation can cause the formation of very large particles, which may lead to an opposite effect (less MPI performance).[35] We found that the GIONF and ferucarbotran signal amplitudes were lower in tissues than in PBS. The MNP signal for PBS was included in the plots for comparison with the signal in tissues. As shown in Fig. 5, the compressibility of various tissues shows minimal variation, resulting in a near-similar response in MPI signal amplitude. This experiment demonstrates that the signal amplitude of tissues containing a specific quantity of MNPs can differ from that of PBS (0% gelatin).

Ota *et al.* demonstrated that dipole interactions diminished the magnetization originating from the Néel relaxation regime, while the Brownian relaxation remained unaffected.[36] Consistent with these findings, our results indicate that the MPI signal of ferucarbotran (with a larger external rotational component) in the tissues decreased less (lower regression) compared to GIONF for both 100 and 500 μg Fe per mL.

Several studies have investigated the microscopic effects of structural variations on MPI signal and relaxation. Arami *et al.* examined how the size of magnetic nanoparticles influences their ferrohydrodynamic relaxometry behavior in different environments, revealing that smaller particles showed faster relaxation times due to increased Brownian motion, which in turn affects the MPI signal quality and resolution.[37] Another study focused on relaxation-based viscosity mapping for MPI, highlighting the impact of environmental viscosity on the relaxation behavior of magnetic nanoparticles. This research developed methods to map viscosity variations, reporting that higher viscosity environments slowed down the relaxation times, which are crucial for diagnostic applications where tissue viscosity is a factor.[9]

Relaxation-based color MPI for viscosity mapping has been introduced previously, enabling the visualization of viscosity variations through color differentiation, thus enhancing the diagnostic capabilities of MPI by allowing for more precise mapping of tissue properties.[18] In addition, another study measured molecular binding using the Brownian motion of magnetic nanoparticle probes. This approach provided a method to quantify molecular interactions and binding events by analyzing the Brownian motion of nanoparticles, offering valuable insights into molecular binding processes in biological systems and improving MPI specificity by showing that bound particles had different relaxation characteristics compared to free particles.[38] Collectively, these studies together with ours deepen the understanding of how structural and environmental factors may influence the MPI signal and particle relaxation behavior, contributing to the enhancement of MPI's diagnostic accuracy and functional imaging capabilities.

The signal FWHM, an indicator for MP image spatial resolution,[39] decreased by increasing the compressibility/decreasing viscosity of gelatin phantoms. The same results were obtained for BSA, while the FWHM was independent of MNP concentration. MNPs produced a signal with higher FWHM in tissues than in water. This most likely results from reduced external rotational motion in a higher viscous matrix (lower compressibility). Our results showed that the change in MPI signal amplitude and FWHM did not depend on the hydrogel type as the MNP signal decreased in both increasing BSA and gelatin samples. Future studies investigating ionic interactions (chemical binding) between MNPs and the matrix components (gelatin, BSA) using inorganic salt solutions with different ionic strengths (*e.g.*, NaCl, $CaCl_2$) may be warranted. This will deepen our understanding of how ionic structures influence nanoparticle behavior and MPI performance, building on the macroscopic compressibility/viscosity analysis to offer a better understanding of the factors influencing the magnetic response and imaging outcomes.

Temperature was shown to influence the magnetic relaxation behavior of MNPs. As the temperature increases, the produced thermal energy enhances the Brownian motion of MNPs. This increased motion can lead to faster relaxation, resulting in a decrease in the magnetic relaxation signal. The nanoparticles become more mobile, which can reduce their alignment and coherence.[40,41] Moreover, elevated temperatures can also affect the interactions between MNPs and the surrounding matrix or tissue. Temperature changes can alter the physical properties of the matrix, such as its compressibility/viscosity, which in turn affects the relaxation behavior of the MNPs and the resulting signal intensity.[42,43] Temperature impacts MPI resolution by increasing Brownian like motion, which reduces magnetic core alignment and coherence, leading to increased FWHM. Additionally, higher temperatures lower saturation magnetization, decreasing the MPI signal and further broadening FWHM. According to the Langevin model, the signal amplitude would scale with magnetization, while resolution would inversely relate to the ratio of magnetization and thermal energy. Both aforementioned factors contribute to reduced resolution, emphasizing the need to account for temperature effects in interpreting MPI performance.[44,45]

Hence, MPI relaxometry could possibly be used to monitor temperature when performing (magneto)thermal therapy. This approach can leverage the time-dependent relaxation of magnetization of MNPs to assist with properly controlling the temperature. Studies have shown that the magnetization response of MNPs, when subjected to an alternating magnetic field (AMF), can be used to extract temperature information due to the temperature-dependent nature of both Brownian and Néel relaxation processes.[46] This approach may achieve two key objectives. First, it may be applied to monitor the temperature of the target during thermal ablation treatment: by exploiting the relationship between the MPI signal and temperature, this method provides real-time monitoring of the target temperature. Second, it may be applied to regulate the heating process. The magnetic heating process can be controlled here by adjusting the magnetic field or the applied frequency. This regulation ensures that the maximum temperature, as measured with MPI, does not exceed safe limits, thereby protecting normal tissues from thermal damage.[5,6,8] However, it is important to note that hysteresis can significantly influence the magnetic response of large particles, especially under AMF conditions used for (MFH) (100–300 kHz). Néel processes, which involve magnetic hysteresis, typically dominate at these high frequencies, impacting the accuracy of temperature measurements if not properly accounted for.[47] The complexities introduced by hysteresis necessitate a robust physical model and thorough calibration to ensure accurate temperature control during MFH.

For FWHM, the effect of temperature increase is less straightforward to interpret. Temperature variations can potentially influence clustering or aggregation of MNPs within the matrix. The degree of clustering in turn can impact the spatial distribution of MNPs and thus affect the FWHM. However, the specific relationship between temperature and FWHM in MPI may depend on MNP properties, matrix characteristics, and imaging parameters.[48,49] Our results are in good agreement with those of Bui *et al.*, who showed FWHM increases with increasing the matrix temperature.[50]

Overall, our results call for correction factors when using MNP calibration samples at a different (*e.g.* room) temperature for *in vivo* applications such as MFH. On the other hand, one may be able to take advantage of this interdependence in that the MPI signal intensity may be used as a non-invasive surrogate temperature probe in MFH. Further detailed studies will be needed to calculate a correction factor for the MPI signal obtained from tissues with different compressibilities, viscosities and temperatures for MPI-guided MFH and other applications.

Experimental

MNP formulations

NF and GIONF were prepared as previously described.[21,22] Briefly, NF consists of small monocrystalline maghemite (γ-Fe_2O_3) grains of 11 nm assembled in a flower-shaped structure, coated with citrate anions. GIONF was synthesized by grafting gold nanoparticles (AuNPs, 2–3 nm) coated with dithiolated diethylenetriaminepentaacetic acid (Au@DTDTPA) onto NF particles. The mean number of AuNPs per NF structure was estimated to be 28 (small NF structures) to 49 (large NF structures). Ferucarbotran (Resovist®), a commercial formulation containing 4.2 nm MNP cores coated with carboxydextran, was purchased from Meito Sangyo Co. Ltd, Japan. FluidMAG-D was purchased from Chemicell (Berlin, Germany). The physical and hydrodynamic size of the MNP formulations was measured with TEM (Hitachi 7600, Ibaraki, Japan) and DLS (Malvern Instruments Ltd, UK), respectively, at 25 °C.

Preparation of MNP-gelatin phantoms

Gelatin (G-6144 from porcine skin, type A) was purchased from Sigma-Aldrich (St. Louis, MO, USA). Phantoms with gelatin concentrations of 1, 2, 4, and 8% w/v were prepared by adding the required amount of dry gelatin powder to deionized (DI) water and stirring at 50 °C for 20 min to ensure homogenous solubilization. MNPs were then added to achieve final concentrations of 0, 25, 50, and 100 μg Fe per mL. Five hundred μL of gelatin-MNP solutions was pipetted into Eppendorf microtubes (PCR tubes) and stored at 4 °C for 24 h to solidify. The same samples were also prepared in DI water (0% w/v gelatin). Three independent pipettings were performed for each MNP sample. The MNP volume being transferred to the gelatin solution was in the range of 5 to 20 μL to ensure accurate iron concentrations in the final samples.

Preparation of MNP-BSA hydrogel phantoms

MNP-containing BSA gel phantoms were prepared using a heat-induced crosslinking method.[51] In brief, 100 μL PBS (containing 270 mM NaCl) solutions containing 10 μg of ferucarbotran or 5 μg of GIONF were prepared with different BSA concentrations (1.5, 2, 3, 4, and 5% w/v BSA). The mixtures were then heated at 75 °C for 40 minutes to induce gel formation. For compressibility measurements, samples containing 30, 40, 60, 80, or 100 mg BSA were prepared in 2 mL PBS (NaCl = 270 mM) and then transferred to 12-well plates (inner height = 9 mm), followed by heating at 75 °C for 40 minutes to induce gel formation.

Preparation of MNP-tissue phantoms

Halal (to minimize blood content) goat brain, lamb liver, lamb kidney, chicken muscle, and cow muscle were purchased from a local grocery shop (Basil Grocery, Hillsborough, NJ, USA) and cut in 50 mm slices. Twenty μL of GIONF (100 μg Fe per mL) or ferucarbotran (500 μg Fe per mL) was injected using a Hamilton syringe (700 Series, Hamilton CO, USA). No backflow leakage was observed after injection.

MPI relaxometry

Magnetic relaxation measurements were performed using an MPI Momentum scanner (Magnetic Insight, Alameda, CA, USA) operating at an excitation frequency of 45 kHz and an RF amplitude of 20 mT. The phantoms were placed at the center of the magnetic field (field-free region). Using the RELAX software module, the point spread function of each sample was determined to characterize both MPI signal amplitude and the full width at half maximum (FWHM). Each measurement took ∼1.5 min. All measurements were repeated three times using triplicate samples.

Compressibility measurements

To determine the compressibility of gel phantoms and tissues, we first measured their ultrasound velocity. The ultrasound waves at 5 MHz (fixed frequency) were measured for gelatin, BSA hydrogel phantoms, and tissues using an ultrasonic thickness gauge with an accuracy of 0.045 mm. The ultrasound gauge contains an ultrasonic probe containing two transmitter and receiver transducers (wintact WT100A, Shenzhen, China). The ultrasound velocity was calculated by:

$$c = \frac{2x}{t} \tag{1}$$

where c is the ultrasonic wave velocity in the object, t is the time between transmitting and receiving the ultrasonic wave, and x is the (known) thickness of the object.

The ultrasonic wave velocity (c) depends on the bulk modulus K and shear modulus G and can be calculated by:

$$c = \left(\frac{K + \frac{4}{3}G}{\rho}\right)^{\frac{1}{2}} \tag{2}$$

Since the shear modulus is zero in fluids and the gel phantoms consist mainly of water, it can be considered negligible.[52,53] The compressibility β_s is defined as the inverse of the bulk modulus K, *i.e.*, $\beta_s = 1/K$. Hence, the ultrasonic wave velocity can be reformulated to:

$$c = (\rho\beta_s)^{-1/2} \tag{3}$$

where ρ is the density and β_s is the compressibility of the gel phantoms which is the inverse of the bulk modulus:

$$\beta_s = 1/\rho c^2 \tag{4}$$

Viscosity measurements

The viscosity of 1, 2, 4, and 8% w/v gelatin and 1.5, 2, 3, 4, and 5% w/v BSA hydrogel samples was measured using a rotational rheometer (MCR 302, Anton Paar, Graz, Austria). For the characterization of the hydrogel samples, the rheometer was configured with a 25 mm parallel plate geometry. The viscosity was determined within a shear rate range of 0.1 to 5 s^{-1} for both gelatin and BSA hydrogel samples. The viscosity values of the gelatin and BSA hydrogel samples were determined in triplicates, with each value measured from an independently prepared hydrogel. Values are reported as mean and standard deviation across the three measurements.

MPI signal amplitude measurements in glycerol and water

To investigate the effect of matrix viscosity on MPI signal amplitude and spatial resolution, 5 μL ferucarbotran in water was mixed with glycerol (99.5%, Sigma-Aldrich G-9012-1L, St. Louis, MO, USA) to make final concentrations of 25, 50, and 100 μg Fe per mL. The samples (total volume of 500 μL) were placed at the center of the magnetic field and MPI signal measurements were obtained using a Momentum scanner (Magnetic Insight, Alameda, CA, USA) operating at an excitation frequency of 45 kHz and an RF amplitude of 20 mT.

Liquid *vs.* dried MNP MPI signal measurements

The magnetic relaxation (PSF function) of GIONF, ferucarbotran, and fluidMAG-D (50 nm, Chemical, Germany) either in solution (100 μg Fe per mL in DI water) or lyophilized (Labconco, MO, USA) dried powder were measured using the RELAX software module. FluidMAG-D was used as a reference MNP formulation as it does not contain a Brownian-like rotation dynamic component.[23] The specific rate of these dynamics was then calculated by dividing the MPI signal amplitude of dried powder by that of the solution.

Temperature measurements

A holder containing two openings for securely locating two 100 μL microtubes was custom printed (Ultimaker 3 Extended 3D Printer, MatterHackers, York, PA, USA) using UltiMaker polylactic acid (PLA) filament (MatterHackers, York, PA, USA) (ESI Fig. 5†). One microtube contained ferucarbotran (100 μg Fe per mL) and the other one DI water for temperature measurements using an inserted fiberoptic thermometer (Fiber Optic Temperature Sensor, type A, SA Instruments, Inc., Stony Brook, NY, USA). The temperature of the microtubes was adjusted through a temperature-controlled water bath with circulating pump (Thermo Scientific SC 150L, Waltham, MA, USA) connected to the holder using water tubes. The magnetic relaxation of the samples was measured as a PSF function using the RELAX software module at temperatures from 10 to 55 °C with 5 °C increments. Three measurements were performed at each temperature.

Conclusions

Matrix composition and temperature are critical parameters that may influence the MPI signal amplitude and FWHM response of MNPs. Hence, caution should be taken when inferring *in vivo* MPI data from calibration/reference standards containing simple aqueous solutions at room temperature. By recognizing and taking into account these factors, we may be able to optimize and customize imaging protocols to improve the robustness of *in vivo* MPI signal quantification.

Data availability

All data generated and analyzed are included in this manuscript and the ESI.†

Author contributions

MS conceived and performed the experimental measurements, analyzed data, and wrote the first draft of the manuscript. WW performed experimental measurements on BSA. SR, Gautier Laurent, and RB provided NF and GIONF nanoparticles. PG conceptualized part of the experimental temperature studies. Guanshu Liu supervised the BSA measurements. JWMB acquired funding, conceived and supervised the experiments, and oversaw data acquisition and analysis. All authors read and edited the manuscript.

Conflicts of interest

JWMB is a paid scientific advisory board member and shareholder of SuperBranche. This arrangement has been reviewed and approved by the Johns Hopkins University in accordance with its conflict-of-interest policies. SR is a co-founder of Nano-H and shareholder of Nano-H and NH-TheraguiX. PG is an employee and shareholder of Magnetic Insight. All others have nothing to disclose.

Acknowledgements

This study was funded by grants from the National Institutes of Health (NIH) R01 CA257557, UH2/UH3 EB028904, S10 OD026740, R33 HL161756, R44 CA285064, the French national agency of research (ANR, Agence Nationale de la Recherche) ANR-23-CE18-0016-01, the Maryland Stem Cell Research Foundation (MSCRF) D-5416, and a grant from Philips Healthcare Inc. We thank Dr Adnan Bibic for 3D printing of the holders used for variable temperature experiments, and Alden Murphy for her assistance with the viscosity measurements.

References

1 B. Gleich and J. Weizenecker, Tomographic imaging using the nonlinear response of magnetic particles, *Nature*, 2005, **435**(7046), 1214–1217.
2 J. W. M. Bulte, Superparamagnetic iron oxides as MPI tracers: A primer and review of early applications, *Adv. Drug Delivery Rev.*, 2019, **138**, 293–301.
3 J. W. M. Bulte, *et al.*, Quantitative "hot-spot" imaging of transplanted stem cells using superparamagnetic tracers and magnetic particle imaging, *Tomography*, 2015, **1**(2), 91–97.
4 O. C. Sehl, *et al.*, A perspective on cell tracking with magnetic particle imaging, *Tomography*, 2020, **6**(4), 315–324.
5 Z. W. Tay, *et al.*, Magnetic particle imaging-guided heating *in vivo* using gradient fields for arbitrary localization of magnetic hyperthermia therapy, *ACS Nano*, 2018, **12**(4), 3699–3713.
6 S. Healy, *et al.*, Clinical magnetic hyperthermia requires integrated magnetic particle imaging, *Wiley Interdiscip. Rev.:Nanomed. Nanobiotechnol.*, 2022, **14**(3), e1779.
7 H. Carlton, *et al.*, Ranking magnetic colloid performance for magnetic particle imaging and magnetic particle hyperthermia, *Adv. Funct. Mater.*, 2024, **34**, 2412321.
8 A. Shakeri-Zadeh and J. W. M. Bulte, Imaging-guided precision hyperthermia with magnetic nanoparticles, *Nat. Rev. Bioeng.*, 2024, **2**, DOI: **10.1038/s44222-024-00257-3**.
9 M. Utkur, Y. Muslu and E. U. Saritas, Relaxation-based viscosity mapping for magnetic particle imaging, *Phys. Med. Biol.*, 2017, **62**(9), 3422.
10 A. M. Rauwerdink and J. B. Weaver, Harmonic phase angle as a concentration-independent measure of nanoparticle dynamics, *Med. Phys.*, 2010, **37**(6Part1), 2587–2592.
11 R. Kötitz, *et al.*, Investigation of Brownian and Néel relaxation in magnetic fluids, *J. Magn. Magn. Mater.*, 1999, **201**(1–3), 102–104.
12 L. M. Bauer, *et al.*, Magnetic particle imaging tracers: state-of-the-art and future directions, *J. Phys. Chem. Lett.*, 2015, **6**(13), 2509–2517.
13 R. J. Deissler, Y. Wu and M. A. Martens, Dependence of Brownian and Néel relaxation times on magnetic field strength, *Med. Phys.*, 2014, **41**(1), 012301.
14 S. M. Dadfar, *et al.*, Size-isolation of superparamagnetic iron oxide nanoparticles improves MRI, MPI and hyperthermia performance, *J. Nanobiotechnol.*, 2020, **18**(1), 1–13.
15 S. Ota, *et al.*, Rotation of magnetization derived from Brownian relaxation in magnetic fluids of different viscosity evaluated by dynamic hysteresis measurements over a wide frequency range, *Nanomaterials*, 2016, **6**(9), 170.
16 R. Dannert, *et al.*, Influence of suspension viscosity on Brownian relaxation of filler particles, *Rheol. Acta*, 2017, **56**, 615–622.
17 M. Utkur and E. U. Saritas, Simultaneous temperature and viscosity estimation capability via magnetic nanoparticle relaxation, *Med. Phys.*, 2022, **49**(4), 2590–2601.
18 M. Utkur, Y. Muslu and E. U. Saritas, Relaxation-based color magnetic particle imaging for viscosity mapping, *Appl. Phys. Lett.*, 2019, **115**(15), 152403.
19 K. Kaczmarek, *et al.*, The effect of tissue-mimicking phantom compressibility on magnetic hyperthermia, *Nanomaterials*, 2019, **9**(5), 803.
20 M. McKee, F. Gordaninejad and X. Wang, Effects of temperature on performance of compressible magnetorheological fluid suspension systems, *J. Intell. Mater. Syst. Struct.*, 2018, **29**(1), 41–51.
21 P. Hugounenq, *et al.*, Iron oxide monocrystalline nanoflowers for highly efficient magnetic hyperthermia, *J. Phys. Chem. C*, 2012, **116**(29), 15702–15712.
22 A. Nicolás-Boluda, *et al.*, Photothermal depletion of cancer-associated fibroblasts normalizes tumor stiffness in desmoplastic cholangiocarcinoma, *ACS Nano*, 2020, **14**(5), 5738–5753.
23 T. Yoshida, *et al.*, Evaluation of harmonic signals for the detection of magnetic nanoparticles, *IEEE Trans. Magn.*, 2012, **48**, 3788–3791.
24 J. W. M. Bulte, *et al.*, Frequency dependence of MR relaxation times. II. Iron oxides, *J. Magn. Reson. Imaging*, 1993, **3**(4), 641–648.
25 J. T. Padding, *Statistical Mechanics of Liquids. Theoretical Chemistry and Spectroscopy Course*, [Online], available: **http://padding.awardspace.info/StatMech-fluids-Padding-part1.pdf**, 2010.
26 W. G. Hoover and F. H. Ree, Melting transition and communal entropy for hard spheres, *J. Chem. Phys.*, 1968, **49**(8), 3609–3617.
27 O. Kaman, *et al.*, Magnetic particle spectroscopy and magnetic particle imaging of zinc and cobalt ferrite nanoparticles–distinct relaxation mechanisms, *J. Alloys Compd.*, 2023, 173022.
28 R. J. Deissler and M. A. Martens, Dependence of the Magnetization Response on the Driving Field Amplitude for Magnetic Particle Imaging and Spectroscopy, *IEEE Trans. Magn.*, 2015, **51**(2), 1–4.
29 K. Takamura, H. Fischer and N. R. Morrow, Physical properties of aqueous glycerol solutions, *J. Pet. Sci. Eng.*, 2012, **98**, 50–60.

30 G. Association, *Physical Properties of Glycerine and its Solutions*, Glycerine Producers' Association, 1963.

31 J. T. Kalathi, *et al.*, Nanoparticle diffusion in polymer nanocomposites, *Phys. Rev. Lett.*, 2014, **112**(10), 108301.

32 D. Eberbeck, *et al.*, Aggregation behaviour of magnetic nanoparticle suspensions investigated by magnetorelaxometry, *J. Phys.: Condens. Matter*, 2006, **18**(38), S2829.

33 L. Maldonado-Camargo, *et al.*, Estimating the contribution of Brownian and Néel relaxation in a magnetic fluid through dynamic magnetic susceptibility measurements, *J. Magn. Magn. Mater.*, 2016, **412**, 223–233.

34 S. Jeon, *et al.*, Quantifying intra-and extracellular aggregation of iron oxide nanoparticles and its influence on specific absorption rate, *Nanoscale*, 2016, **8**(35), 16053–16064.

35 S. M. Dadfar, *et al.*, Size-isolation of superparamagnetic iron oxide nanoparticles improves MRI, MPI and hyperthermia performance, *J. Nanobiotechnol.*, 2020, **18**, 1–13.

36 S. Ota and Y. Takemura, Characterization of Néel and Brownian relaxations isolated from complex dynamics influenced by dipole interactions in magnetic nanoparticles, *J. Phys. Chem. C*, 2019, **123**, 28859–28866.

37 H. Arami, *et al.*, Size-dependent ferrohydrodynamic relaxometry of magnetic particle imaging tracers in different environments, *Med. Phys.*, 2013, **40**(7), 071904.

38 A. M. Rauwerdink and J. B. Weaver, Measurement of molecular binding using the Brownian motion of magnetic nanoparticle probes, *Appl. Phys. Lett.*, 2010, **96**(3), 033702.

39 Z. W. Tay, *et al.*, The relaxation wall: experimental limits to improving MPI spatial resolution by increasing nanoparticle core size, *Biomed. Phys. Eng. Express.*, 2017, **3**(3), 035003.

40 C. N. Obeada and I. Malaescu, The temperature effect on the combined Brownian and Neel relaxation processes in a water-based magnetic fluid, *Phys. B*, 2013, **424**, 69–72.

41 R. Regmi, *et al.*, Temperature dependent dissipation in magnetic nanoparticles, *J. Appl. Phys.*, 2014, **115**(17), 17B301.

42 R. A. Fine and F. J. Millero, Compressibility of water as a function of temperature and pressure, *J. Chem. Phys.*, 1973, **59**(10), 5529–5536.

43 F. J. Millero, R. W. Curry and W. Drost-Hansen, Isothermal compressibility of water at various temperatures, *J. Chem. Eng. Data*, 1969, **14**(4), 422–425.

44 J. Wells, *et al.*, Temperature dependence in magnetic particle imaging, *AIP Adv.*, 2018, **8**, 056703.

45 C. Caizer and I. Hrianca, The temperature dependence of saturation magnetization of γ-Fe2O3/SiO2 magnetic nanocomposite, *Ann. Phys.*, 2003, **515**(1–2), 115–122.

46 J. B. Weaver, A. M. Rauwerdink and E. W. Hansen, Magnetic nanoparticle temperature estimation, *Med. Phys.*, 2009, **36**(5), 1822–1829.

47 P. Bender, *et al.*, Relating magnetic properties and high hyperthermia performance of iron oxide nanoflowers, *J. Phys. Chem. C*, 2018, **122**(5), 3068–3077.

48 Z. W. Tay, *et al.*, Optimization of drive parameters for resolution, sensitivity and safety in magnetic particle imaging, *IEEE Trans. Med. Imaging*, 2019, **39**(5), 1724–1734.

49 K. H. Yeo, *et al.*, Characterizing the performance of commercial magnetic particles for magnetic particle imaging, *Int. J. Magn. Part. Imaging*, 2022, **8**(1 Suppl 1), 203080.

50 T. Q. Bui, *et al.*, Harmonic dependence of thermal magnetic particle imaging, *Sci. Rep.*, 2023, **13**(1), 15762.

51 M. Murata, *et al.*, Heat-induced Transparent Gel Formation of Bovine Serum Albumin, *Biosci., Biotechnol., Biochem.*, 1993, **57**(1), 43–46.

52 K. Manickam, R. R. Machireddy and S. Seshadri, Characterization of biomechanical properties of agar based tissue mimicking phantoms for ultrasound stiffness imaging techniques, *J. Mech. Behav. Biomed. Mater.*, 2014, **35**, 132–143.

53 D. Li, *et al.*, The effect of fluid saturation on the dynamic shear modulus of tight sandstones, *J. Geophys. Eng.*, 2017, **14**(5), 1072–1086.